








# Metal-oxygen decoordination stabilizes anion redox in Li-rich oxides

Jihyun Hong <sup>1,2,3,4,11,12</sup>, William E. Gent <sup>5,6,12</sup>, Penghao Xiao<sup>7</sup>, Kipil Lim<sup>1,2,3,4</sup>, Dong-Hwa Seo <sup>8</sup>, Jinpeng Wu<sup>3,6</sup>, Peter M. Csernica<sup>1</sup>, Christopher J. Takacs<sup>2</sup>, Dennis Nordlund<sup>2</sup>, Cheng-Jun Sun<sup>9</sup>, Kevin H. Stone <sup>2</sup>, Donata Passarello<sup>2</sup>, Wanli Yang <sup>6</sup>, David Prendergast <sup>10</sup>, Gerbrand Ceder<sup>7,8\*</sup>, Michael F. Toney <sup>2,4\*</sup> and William C. Chueh <sup>1,3,4\*</sup>

**Reversible high-voltage redox chemistry is an essential component of many electrochemical technologies, from (electro)catalysts to lithium-ion batteries. Oxygen-anion redox has garnered intense interest for such applications, particularly lithium-ion batteries, as it offers substantial redox capacity at more than 4 V versus Li/Li<sup>+</sup> in a variety of oxide materials. However, oxidation of oxygen is almost universally correlated with irreversible local structural transformations, voltage hysteresis and voltage fade, which currently preclude its widespread use. By comprehensively studying the Li<sub>2-x</sub>Ir<sub>1-y</sub>Sn<sub>y</sub>O<sub>3</sub> model system, which exhibits tunable oxidation state and structural evolution with y upon cycling, we reveal that this structure-redox coupling arises from the local stabilization of short approximately 1.8 Å metal-oxygen π bonds and approximately 1.4 Å O–O dimers during oxygen redox, which occurs in Li<sub>2-x</sub>Ir<sub>1-y</sub>Sn<sub>y</sub>O<sub>3</sub> through ligand-to-metal charge transfer. Crucially, formation of these oxidized oxygen species necessitates the decoordination of oxygen to a single covalent bonding partner through formation of vacancies at neighbouring cation sites, driving cation disorder. These insights establish a point-defect explanation for why anion redox often occurs alongside local structural disordering and voltage hysteresis during cycling. Our findings offer an explanation for the unique electrochemical properties of lithium-rich layered oxides, with implications generally for the design of materials employing oxygen redox chemistry.**

Reversible redox chemistry in solids under highly oxidizing conditions (for example versus H<sub>2</sub>/H<sup>+</sup>, Li/Li<sup>+</sup> or O<sub>2</sub>) is a powerful tool in (electro)chemical systems, increasing the catalytic activity of oxygen evolution and methane functionalization (electro)catalysts as well as the energy and power densities of lithium-ion batteries (LIBs)<sup>1</sup>. In LIBs in particular, employing high-voltage redox has been identified as a promising avenue to meeting the energy density demands of next-generation technologies such as plug-in electric vehicles.

Recently, anionic oxygen redox has been shown to offer access to substantial high-voltage (de)intercalation capacity in a range of electrode materials<sup>2–7</sup>, spurring an intense research effort to understand this phenomenon. While many oxygen-redox-active materials have been developed, they almost universally exhibit a host of irreversible electrochemical behaviours such as voltage hysteresis and voltage fade<sup>8</sup>. This is most notable in the anion-redox-active Li-rich layered oxides, Li<sub>1+x</sub>M<sub>1-x</sub>O<sub>2</sub> (M is a transition metal (TM) or non-TM such as Al, Sn or Mg), which exhibit capacities approaching 300 mAh g<sup>-1</sup> but have yet to achieve commercial success due to such electrochemical behaviours<sup>5,9</sup>. It has been shown both experimentally<sup>10–12</sup> and from first-principles thermodynamics<sup>13</sup> that the migration of M into empty Li sites<sup>9</sup>—creating structural disorder in the form of M<sub>Li</sub>–V<sub>M</sub> antisite–cation–vacancy point-defect pairs—is at the root of voltage profile evolution and depression, particularly

during the first cycle. Oxygen redox has separately been shown to trigger voltage hysteresis and sluggish kinetics<sup>3,14</sup>, with the implication being that oxygen redox and TM migration–vacancy formation are often intrinsically linked. Indeed, coupling between oxygen redox, cation migration and voltage hysteresis was recently observed<sup>6</sup>. However, under the two primary models that have emerged to describe the nature of the lattice oxygen in these materials (either an approximately 2.5 Å peroxy-like O<sub>2</sub><sup>n-</sup> dimer<sup>3,15</sup> or an isolated O<sup>-</sup> anion<sup>4,5,16</sup>), it is unclear as to why the oxidation of oxygen should lead to the correlated structural transformations and voltage hysteresis. It has been argued qualitatively that the oxidation of oxygen destabilizes the layered structure<sup>2,15</sup>; however, a robust understanding of the materials design criteria for achieving structurally and electrochemically reversible anion redox remains elusive.

In approaching this issue, we turn to layered Li<sub>2</sub>IrO<sub>3</sub> (equivalently, Li[Li<sub>0.33</sub>Ir<sub>0.67</sub>]O<sub>2</sub> or LIO), which is reported to exhibit anion redox, yet unlike other Li-rich layered oxides exhibits highly reversible structural and electrochemical behaviour during cycling<sup>15,17</sup>. Upon substituting redox-inactive Sn for Ir, the solid-solution material Li<sub>2</sub>Ir<sub>1-y</sub>Sn<sub>y</sub>O<sub>3</sub> (LISO) forms M<sub>Li</sub>–V<sub>M</sub> defects during charge, accompanied by voltage hysteresis during subsequent cycling that is typical of other anion-redox-active oxides<sup>15</sup>. This tunability makes LIO/LISO an ideal model system for studying the link between anion redox, local structure and irreversible electrochemistry.

<sup>1</sup>Department of Materials Science and Engineering, Stanford University, Stanford, CA, USA. <sup>2</sup>Stanford Synchrotron Radiation Lightsource, SLAC National Accelerator Laboratory, Menlo Park, CA, USA. <sup>3</sup>Stanford Institute for Materials & Energy Sciences, SLAC National Accelerator Laboratory, Menlo Park, CA, USA. <sup>4</sup>Applied Energy Division, SLAC National Accelerator Laboratory, Menlo Park, CA, USA. <sup>5</sup>Department of Chemistry, Stanford University, Stanford, CA, USA. <sup>6</sup>The Advanced Light Source, Lawrence Berkeley National Laboratory, Berkeley, CA, USA. <sup>7</sup>Materials Sciences Division, Lawrence Berkeley National Laboratory, Berkeley, CA, USA. <sup>8</sup>Department of Materials Science and Engineering, University of California, Berkeley, CA, USA. <sup>9</sup>The Advanced Photon Source, Argonne National Laboratory, Lemont, IL, USA. <sup>10</sup>The Molecular Foundry, Lawrence Berkeley National Laboratory, Berkeley, CA, USA.

<sup>11</sup>Present address: Center for Energy Materials Research, Korea Institute of Science and Technology (KIST), Seoul, Republic of Korea.

<sup>12</sup>These authors contributed equally: Jihyun Hong, William E. Gent. \*e-mail: [gceder@berkeley.edu](mailto:gceder@berkeley.edu); [mftoney@slac.stanford.edu](mailto:mftoney@slac.stanford.edu); [wchueh@stanford.edu](mailto:wchueh@stanford.edu)

In this work, we show that the difference in electrochemical and structural behaviour between LIO and LISO holds the key to understanding anion redox. Using a combination of bulk-sensitive spectroscopic and structural probes in conjunction with first-principles calculations, we demonstrate that anion redox only occurs simultaneously with structural disordering (that is, antisite–vacancy formation) in LISO, and is completely absent from LIO up to 4.6 V, further establishing the strong coupling between these two phenomena. We demonstrate that the approximately 2.5 Å O–O dimers that form in LIO do not constitute oxidized oxygen, and that the high degree of covalency and the low voltage of the Ir redox states together prevent oxygen redox from being accessed in LIO. Crucially, we reveal the origin of the coupling between structural evolution and oxygen redox in LISO using density functional theory (DFT) calculations, wherein the low valence-electron count in delithiated LISO promotes charge transfer from O to Ir (essentially, oxygen oxidation via ligand-to-metal charge transfer, or LMCT) through drastic changes in the local bonding configuration. We identify two main bonding configurations that are able to stabilize both the low valence-electron count through LMCT and the resulting oxidized oxygen species: short approximately 1.8 Å Ir–O  $\pi$  bonds (equivalently, terminal Ir=O oxo species) and short approximately 1.4 Å O–O dimers. Both configurations require the decoordination of oxygen to a single covalent bonding partner, which is realized in the layered structure through vacancy formation due to in-plane and out-of-plane site disorder (cation migration). Meanwhile, the higher valence-electron count in LIO disfavours LMCT and thus LIO exhibits minimal structural disordering, cation redox only and more reversible electrochemistry. While further investigation is needed to understand how this mechanism depends on the nature of the TM, this point-defect model can offer a causal explanation for the nearly universal observation of structural and electrochemical irreversibility in anion-redox-active Li-rich materials, and reveals previously unconsidered design parameters through which to improve them, such as the electronic and structural mechanism of LMCT and oxygen decoordination. These principles apply generally to the design of the broad class of highly oxidized oxides where anion redox is likely to play a role.

### Electrochemistry and phase behaviour of LIO

As previously reported<sup>15,17</sup>, Fig. 1a shows that LIO exhibits two well-defined voltage plateaus with average potentials of 3.45 V and 4.15 V versus Li/Li<sup>+</sup> and a total capacity of 1.5 e<sup>−</sup> per Ir. It has been shown that LIO exhibits a layered structure with monoclinic *C2/m* symmetry, with the Li and TMs in the TM layers ordered into a honeycomb-like arrangement, and accommodates delithiation through changes in the stacking of the TM layers, changing from initially O3 to O1<sup>18</sup> at the end of charge. This is further supported here by Rietveld refinement of the synchrotron X-ray diffraction (XRD) patterns (Supplementary Figs. 1 and 2, Supplementary Tables 1 and 2 and Supplementary Discussion 1). In addition, we identify the intermediate Li<sub>1</sub>IrO<sub>3</sub> phase as exhibiting T3 stacking using DFT (Supplementary Fig. 3). We note that the material studied here exhibits a high degree of initial structural ordering and electrochemical reversibility, and is therefore more similar to that reported by Kobayashi et al.<sup>17</sup> than McCalla et al.<sup>15</sup>

While it has been shown that LIO exhibits minimal structural disordering during the first charge, for this study it is important to quantify the cation vacancy–antisite formation during electrochemical cycling such that it can be compared with that of LISO. We employed an iterative approach to simultaneously refine the in-plane and out-of-plane site disorder as described in Supplementary Discussion 1 and Supplementary Fig. 4. This approach eliminates the difficulty in site occupancy determination resulting from the presence of stacking faults. We confirm the absence of V<sub>Ir</sub>–Ir<sub>Li</sub> defects ( $\leq 0.1 \pm 0.2\%$  of all Li sites occupied by Ir) in the discharged

state both before and after the first electrochemical cycle. In-plane site occupancy refinement of the fully charged O1 structure is challenging due to distortions to the oxygen sublattice<sup>15</sup> and the absence of superstructure peaks. However, out-of-plane refinement shows negligible Ir occupancy in the Li layer in the fully charged state. Consistently, DFT calculations indicate that in-plane and out-of-plane Ir antisite–vacancy defect pairs in the fully charged state have a positive formation energy of +0.49 and +0.20 eV (per Li<sub>4</sub>Ir<sub>8</sub>O<sub>24</sub> supercell), respectively. Together, these results show why LIO exhibits reversible electrochemistry: minimal cation disordering occurs during cycling. This is unlike most other Li-rich materials in which anion redox is reported to occur<sup>7,9,12,19</sup>.

### Multivalent iridium redox in LIO

The nature of anion redox in LIO should therefore be examined with further scrutiny. In addition, a strict definition of anion redox is needed. Until now, oxygen redox has been defined as the depopulation of non-bonding (or ‘weakly/minimally hybridized’) oxygen 2*p* states<sup>5,6,16,20,21</sup>. However, this definition does not take into account how materials respond to the depopulation of these states, which as we will show later is a crucial component of oxygen redox. So, we provide a more specific definition here: oxygen redox requires the depopulation of non-bonding (or weakly/minimally hybridized) oxygen 2*p* states wherein the resulting holes reside in predominantly oxygen character orbitals after any structural and electronic reorganization has occurred. A previous study reported anion redox in LIO based on (a) surface-sensitive X-ray photoelectron spectroscopy showing the appearance of an oxygen state with reduced electron density and (b) neutron diffraction and transmission electron microscopy measurements showing the contraction of the octahedral O–O distance from about 2.7 Å to about 2.5 Å<sup>15</sup>. Here we use bulk-sensitive X-ray spectroscopic techniques to directly determine the nature of the hole states formed during charge and, by induction, the redox processes in LIO. We first show in Fig. 1 analysis of the operando transmission X-ray absorption near edge structure (XANES) at the Ir L<sub>3</sub> edge during the first cycle of LIO<sup>19,22,23</sup>. Fig. 1b shows that the white-line (WL) energy increases linearly during the galvanostatic charge up to Li<sub>0.5</sub>IrO<sub>3</sub> and then decreases linearly on discharge, nearly returning to its original value after the full cycle. Fig. 1c, meanwhile, shows that the WL intensity increases up to Li<sub>1</sub>IrO<sub>3</sub> but then decreases when charging further to Li<sub>0.5</sub>IrO<sub>3</sub>, with the trend reversing on discharge. Principal-component analysis and non-negative matrix factorization of the XANES spectra (Supplementary Discussion 2 and Supplementary Fig. 5) reveal the presence of three spectral end members corresponding to the Li<sub>2</sub>IrO<sub>3</sub>, Li<sub>1</sub>IrO<sub>3</sub> and Li<sub>0.5</sub>IrO<sub>3</sub> compositions, consistent with the presence of two isosbestic points. These three end-member spectra (Fig. 1d, inset) reflect the observed changes, with Li<sub>0.5</sub>IrO<sub>3</sub> having the highest WL energy followed by Li<sub>1</sub>IrO<sub>3</sub> and Li<sub>2</sub>IrO<sub>3</sub>, and with Li<sub>1</sub>IrO<sub>3</sub> having the strongest WL peak intensity. A linear combination analysis using these end members confirms that the entire spectral evolution is well described by two consecutive two-phase reactions between Li<sub>2</sub>IrO<sub>3</sub> and Li<sub>1</sub>IrO<sub>3</sub>, and between Li<sub>1</sub>IrO<sub>3</sub> and Li<sub>0.5</sub>IrO<sub>3</sub> (Fig. 1d and Supplementary Fig. 5).

To understand what these spectral changes indicate, we note that the L<sub>3</sub> WL energy has been shown to vary linearly with formal Ir oxidation state<sup>24</sup>. Thus the linear trend during galvanostatic cycling indicates a linear, monotonic change in Ir oxidation state, with a total WL shift of 1.2 eV. The Ir WL energy difference between Ir<sup>6+</sup> and Ir<sup>4+</sup> compounds is typically between 1.4 and 2.0 eV<sup>23,24</sup>, and the WL shift here is therefore consistent with Ir being oxidized by between 1.2 and 1.7 e<sup>−</sup>. Although it was argued that a loss in WL intensity indicates Ir reduction in Li<sub>3</sub>IrO<sub>4</sub><sup>19</sup>, it has been shown that the WL intensity of Ir<sup>6+</sup> is lower than that of Ir<sup>5+23,24</sup>, which may be due to the WL intensity becoming dominated by relaxation quenching rather than d count for d counts below d<sup>4</sup>–d<sup>5</sup><sup>25</sup>. Thus both the

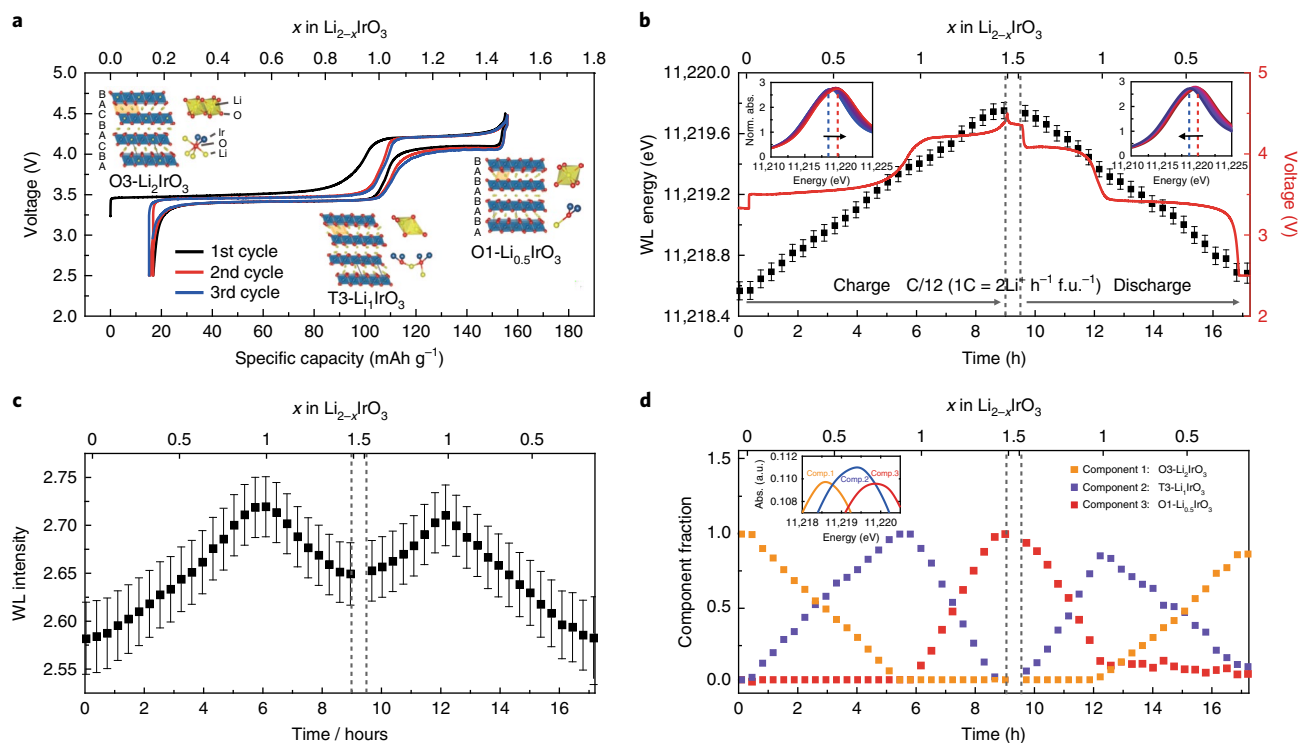


**Fig. 1 | Reversible multivalent iridium redox in  $\text{Li}_{2-x}\text{IrO}_3$ .** **a**, Capacity–voltage curves of  $\text{Li}_{2-x}\text{IrO}_3$  galvanostatically measured at a C/12 rate ( $17.58 \text{ mA g}^{-1}$ ) between 4.50 and 2.50 V for the initial three cycles. The stable phases during the two consecutive two-phase reactions of  $\text{Li}_{2-x}\text{IrO}_3$  occurring at each voltage plateau, obtained by combined XRD Rietveld refinements and DFT calculations, are shown. **b**, Evolution of the  $\text{Ir L}_3$  WL energy (black squares) during the first cycle, measured through operando transmission XAS, showing the continuous oxidation–reduction of iridium throughout the whole charge–discharge processes. The raw XANES data for charging and discharging are shown in the left and right insets, respectively. **c**, Evolution of the  $\text{Ir L}_3$  WL intensity, showing the highest intensity at the  $\text{Li}_2\text{IrO}_3$  composition, where Ir is in the 5+ oxidation state. It is known that  $\text{Ir}^{5+}$  has a higher WL intensity than  $\text{Ir}^{4+}$  and Ir, and thus the subsequent intensity decay is consistent with further oxidation of  $\text{Ir}^{5+}$  to  $\text{Ir}^{5.5+}$  during the high-voltage plateau at 4.15 V. The error bars in **b** and **c** represent the standard error in fitting each  $\text{Ir L}_3$  XANES spectrum with the sum of an error function and a Lorentzian peak. **d**, Linear combination analysis of non-negative matrix factorization components, showing three distinct  $\text{Ir L}_3$ -edge spectra as end members (inset).

WL energy and intensity suggest a monotonic oxidation of Ir from  $4^+$  to between  $5.2^+$  and  $5.7^+$ .

Since the linear coefficient between WL energy and oxidation state appears to vary slightly between materials<sup>23,24</sup>, it is impossible to precisely quantify the final Ir oxidation state based on XANES studies in other materials. Thus, although the monotonicity of the Ir oxidation is already in striking contrast to the behaviour of most anion redox active Li-rich oxides, whose TM ions either stop being oxidized or are even reduced during the high-voltage plateau<sup>4,6,16</sup>, and suggests the absence of anion redox in LIO and a final Ir oxidation state of  $5.5^+$ , this cannot be proven with XANES alone. To directly assess the contribution of bulk O to the LIO redox mechanism, we perform soft X-ray absorption spectroscopy (sXAS) at the O K edge. Transmission and fluorescence yield (FY) detection modes with probing depths of hundreds of nanometres were employed (see methods). Fig. 2a shows the O K-edge sXAS-FY and transmission sXAS spectra of LIO (initially in the  $t_{2g}^5 e_g^0$  electronic configuration) during the first electrochemical cycle. The peaks at about 529 eV and 532 eV are ascribed to the unoccupied Ir  $5d$ -O  $2p$   $t_{2g}$  and  $e_g^*$  hybridized states, respectively<sup>26,27</sup>. The difference plots taken between different states of charge (Fig. 2b) clearly show that the intensity of the  $t_{2g}$  peak increases and decreases throughout charge and discharge, mirroring the evolution of the Ir  $L_3$  WL (Fig. 1c). Fig. 2c shows that the integrated area ratio of the two O K XAS pre-edge peaks follows the same trend in transmission sXAS, which probes the entirety of the particles, confirming that this is a bulk phenomenon.

The correlated changes at the O K and Ir  $L_3$  edges indicate redox of a hybridized Ir–O state, and are widely accepted as a fingerprint of conventional ‘TM–O’ cation redox<sup>6</sup> observed in a variety of compounds such as  $\text{LiNi}_{0.5}\text{Mn}_{1.5}\text{O}_4$ <sup>28</sup>,  $\text{LiFePO}_4$ <sup>29</sup> and  $3d$  layered TM oxides<sup>6,26</sup>. While in these systems the oxidation of the TM is accompanied by charge sharing with the anions, this clearly does not qualify as oxygen redox according to the earlier definition, since no additional unhybridized O  $2p$  electrons are depopulated beyond the hybridized TM–O states. This is further supported by resonant inelastic X-ray scattering (RIXS) at the O K edge. It has recently been shown that depopulation of unhybridized O  $2p$  states in some Li-rich materials results in a sharp absorption feature at about 530.8 eV excitation energy at the O K edge with a characteristic emission at about 523.0 eV, evident in both RIXS maps<sup>6</sup> and single-energy RIXS spectra<sup>6,16,30,31</sup>, which is distinct from the energy of typical hybridization features in most TM oxides. Fig. 2d shows, however, that no such feature appears even in the fully charged LIO. Thus, in conjunction with the XANES results, O K-edge sXAS and RIXS further support pure multivalent, hybridized Ir–O redox in the absence of oxygen redox in LIO.

This is also supported by DFT calculations. The predicted projected densities of states (pDOSs) of the oxygen  $2p$  and Ir  $5d$  states of the three structures formed during cycling are shown in Fig. 2e. Changes in the Ir and O pDOS as a function of Li stoichiometry show that all states depopulated during delithiation contain both Ir and O character. The unhybridized O  $2p$  states (that is, the non-bonding O  $2p$  band) lie about 2 eV below the Fermi level in  $\text{Li}_{0.5}\text{IrO}_3$

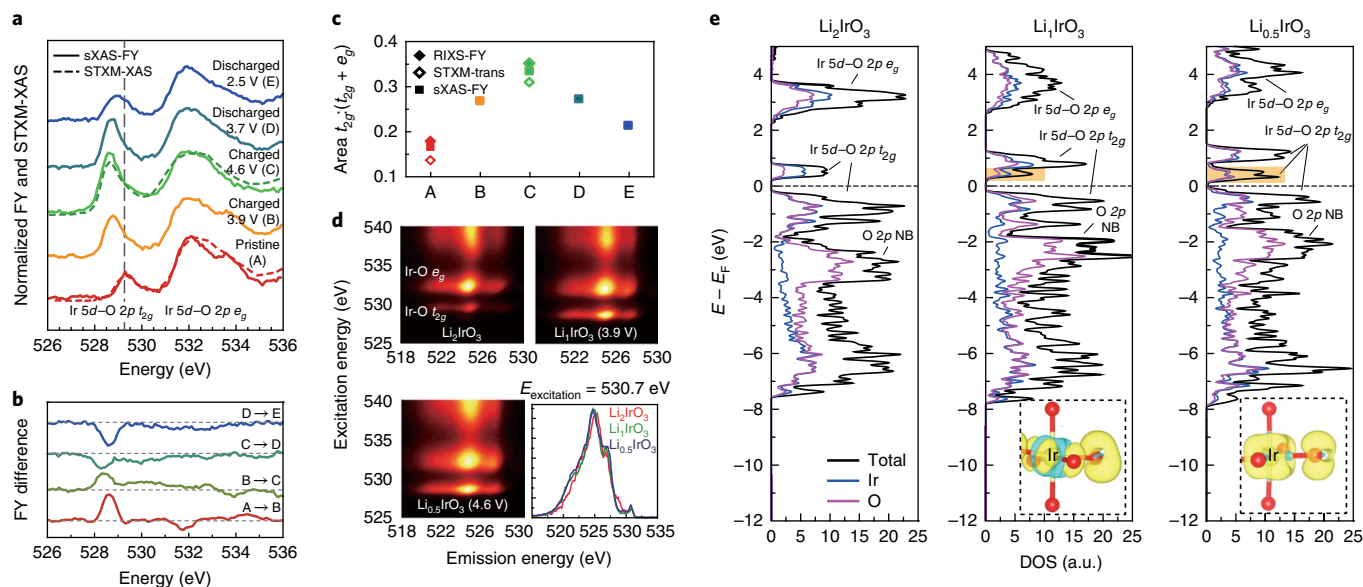


**Fig. 2 | Hybridized Ir–O redox in  $\text{Li}_{2-x}\text{IrO}_3$ .** **a**, sXAS-FY spectra and XAS obtained through scanning transmission X-ray microscopy (STXM-XAS) of the O K edge of  $\text{Li}_{2-x}\text{IrO}_3$  at various voltages throughout the first cycle. From bottom to top, pristine (A), charged to 3.9 V (B), charged to 4.6 V (C), discharged to 3.7 V after being charged to 4.6 V (D) and discharged to 2.5 V after being charged to 4.6 V (E). **b**, Difference plot of sXAS obtained from **a** showing the intensity evolution of Ir  $5d\text{--}O\ 2p\ t_{2g}$  and  $e_g$  peaks. **c**, Ratio of the Ir  $5d\text{--}O\ 2p\ t_{2g}$  peak area to the total Ir  $5d\text{--}O\ 2p\ t_{2g} + e_g$  area measured by RIXS, STXM and sXAS, showing the continuous growth and decay of the  $t_{2g}$  area. The O K-edge measurements were normalized by the intensity at 545 eV after subtracting the background intensity. **d**, O K-edge RIXS maps of  $\text{Li}_2\text{IrO}_3$ ,  $\text{Li}_1\text{IrO}_3$  and  $\text{Li}_{0.5}\text{IrO}_3$ . The bottom right panel shows the RIXS spectra at 530.7 eV excitation energy for each composition where a feature corresponding to anion redox is reported to appear. The intensities are normalized by the TFY intensity at 540 eV. **e**, Ir- and O-projected density of states of  $\text{Li}_2\text{IrO}_3$ ,  $\text{Li}_1\text{IrO}_3$  and  $\text{Li}_{0.5}\text{IrO}_3$  calculated from first principles, demonstrating no access to the buried O 2p non-bonding (NB) states. Insets show the isosurface of the charge density for the lowest unoccupied states corresponding to  $0.5\ e^-$  f.u. $^{-1}$  in  $\text{Li}_1\text{IrO}_3$  and  $\text{Li}_{0.5}\text{IrO}_3$  (shaded region in **e**) visualizing two different Ir  $5d\text{--}O\ 2p\ t_{2g}$  hybridized states. Yellow and blue show negative and positive changes in charge density, respectively. Li ions are omitted for clarity.

and are therefore not emptied. Insets in Fig. 2e plot the isosurface of the spin density of the lowest unoccupied (that is, redox active) states around Ir and O for  $\text{Li}_1\text{IrO}_3$  and  $\text{Li}_{0.5}\text{IrO}_3$  (equivalent to  $0.5\ e^-$  per formula unit (f.u.), shaded in the DOS). In both cases, we observe large spin density around both Ir and O ions in the shape of two distinct hybridized Ir  $5d\text{--}O\ 2p\ t_{2g}$  orbitals—probably  $d_{xy}$  and mixed  $d_{yz}\text{--}d_{xz}$ . Thus, although all oxygen ions in LIO exhibit the linear Li–O–Li structural motif that was recently shown to raise the energy of the O 2p states and promote oxygen redox in many Li-rich materials (see Supplementary Fig. 6)<sup>5,6,32</sup>, these results demonstrate that the Ir<sup>4/5.5+</sup> redox band (where 5.5 denotes the average formal oxidation state) is too high in energy for these labile O 2p states to compete for redox in LIO, similar to predictions made for V, Cr and Mo<sup>5</sup>.

Having employed a suite of bulk-sensitive spectroscopic probes and computation, we show that only hybridized TM–O states are accessed in LIO, with Ir reaching the 5.5<sup>+</sup> formal oxidation state at the end of charge. We therefore re-classify LIO as anion-redox inactive within the 2.5–4.6 V window. In terms of addressing previous conflicting conclusions, it is likely that the oxidized oxygen species observed by X-ray photoelectron spectroscopy are due to near-surface phenomena, which do not play a significant role in the bulk redox mechanism. As for the long approximately 2.5 Å O–O dimers that were observed to form in the bulk of charged LIO, we conclude that these species are not sufficient evidence of oxidized oxygen. This is based on the observation that most TM-coordinated oxidized oxygen dimers are between 1.3 and 1.5 Å in length<sup>33</sup>. We speculate on alternative explanations for the dimerization phenomenon in Supplementary Discussion 3 and Supplementary Fig. 7.

### Charging LISO beyond Ir<sup>5.5+</sup> creates $V_M\text{--}M_{Li}$ defects

When Sn is substituted into LIO to make solid-solution phase LISO, the electrochemistry changes dramatically and becomes typical of that of anion-redox-active materials (Fig. 3a). We use the notation LISO## to represent the compound with ##% Sn content, and the term ‘LISO’ to refer to the Sn-substituted materials generally. Regardless of Sn content, when charged beyond Ir<sup>5.5+</sup> LISO exhibits a new plateau at about 4.35 V, followed by a large voltage drop on subsequent discharge, a permanently sloped voltage profile and voltage hysteresis that persists even at open circuit (Supplementary Fig. 8). Despite the drastic changes to the voltage profile, LISO25 exhibits reasonable capacity retention with cycling (74.5% after 192 cycles, Supplementary Fig. 9). The new high-voltage plateau, in conjunction with the additional reversible capacity well beyond 1.5 e<sup>−</sup> per Ir (Fig. 3a), indicates the presence of a reversible redox partner beyond Ir<sup>4+</sup>/Ir<sup>5.5+</sup>.

In addition to this high-voltage redox partner, the average and local structural behaviour of LISO differs from that of LIO. As first demonstrated by McCalla et al.<sup>15</sup>, a substantial degree of cation site disorder develops in LISO after first delithiation. Fig. 3b quantifies the extent of site disorder in LISO25 before and after electrochemical cycling with either a 4.25 or 4.60 V cutoff. The iterative Rietveld refinement results are shown in Supplementary Fig. 10 and Supplementary Tables 3 and 4. As shown schematically in Fig. 3b, we assume that each in-plane and out-of-plane antisite defect results in a corresponding vacant M site ( $V_M$ ). Since low concentrations of  $\text{Sn}_{Li}$  and  $\text{Ir}_{Li}$  have identical effects on the Bragg peak intensity, XRD cannot be used to differentiate between the migrating species. We therefore perform the refinement assuming either all  $\text{Ir}_{Li}$  for both in-plane and out-of-plane defects or only  $\text{Sn}_{Li}$  for

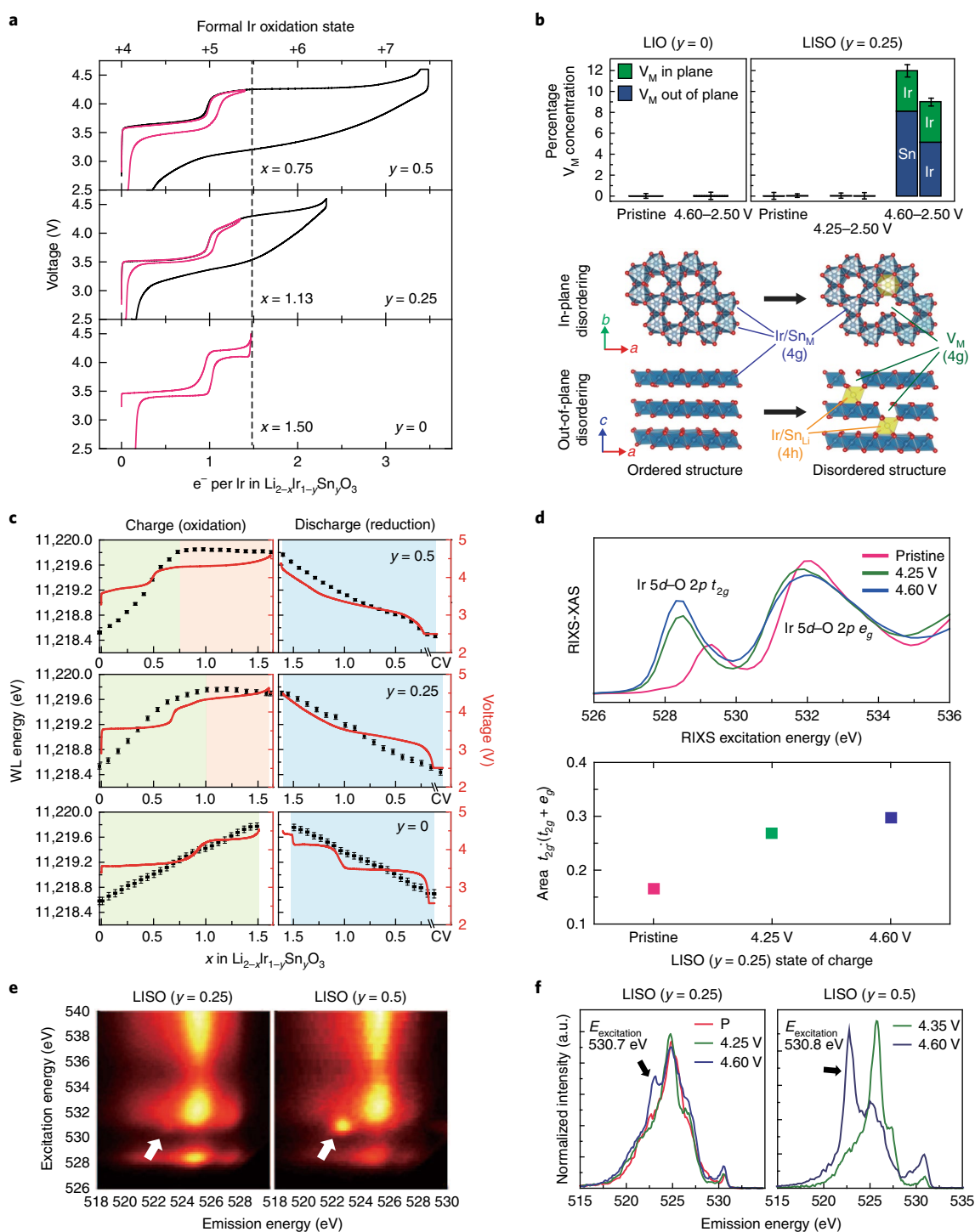


**Fig. 3 | Irreversible electrochemistry, structural disordering, and redox behaviour of  $\text{Li}_{2-x}\text{Ir}_{1-y}\text{Sn}_y\text{O}_3$ .** **a**, Charge-discharge profiles of  $\text{Li}_{2-x}\text{Ir}_{1-y}\text{Sn}_y\text{O}_3$  under a constant current density (C/10 rate) for a full cycle (black) and for an approximately  $1.5 e^-$  per Ir per f.u. cycle (pink). **b**, In-plane and out-of-plane disorder quantified by iterative XRD Rietveld refinement for LISO25 cycled in the 4.60–2.50 V and 4.25–2.50 V windows and LIO cycled in the 4.60–2.50 V window, quantified by the total  $V_M$  concentration. The scheme illustrates the in-plane and out-of-plane structural disordering mechanisms resulting in  $V_M$ , with the migrated cation octahedron shaded yellow and the Wyckoff positions indicated in parentheses. **c**, Operando transmission XANES spectra of the Ir  $L_3$  edge for the first cycle showing the continuous Ir oxidation up to 4.25 V, no shift beyond 4.25 V and the continuous Ir reduction during discharge. CV denotes the region of constant voltage hold at 2.5 V at the end of discharge. The error bars represent the standard error in fitting each Ir  $L_3$  XANES spectrum with the sum of an error function and a Lorentzian peak. **d**, sXAS-FY O K-edge spectra (obtained by integrating the RIXS data onto the excitation axis, RIXS-XAS) throughout the first cycle for LISO25 and the corresponding ratio of the Ir  $5d\text{-O } 2p t_{2g}$  peak area to the total Ir  $5d\text{-O } 2p t_{2g} + e_g^*$  area. **e**, O K-edge RIXS maps of LISO25 and LISO50 charged to 4.60 V showing a localized RIXS feature at 530.7 eV excitation energy and 522.8 eV emission energy. **f**, Single-energy RIXS spectra of LISO25 and LISO50 showing more clearly the anion-redox signature. The intensities are normalized by the TFY intensity at 540 eV.

out-of-plane defects and  $\text{Ir}_{\text{Li}}$  for in-plane defects (assuming all  $\text{Sn}_{\text{Li}}$  for both types of defect leads to full depletion of the Sn content in the M sites in LISO25). We quantify the total amount of disorder by the fraction of  $V_{\text{M}}$ , which reaches between  $9.0 \pm 0.9\%$  (assuming all  $\text{Ir}_{\text{Li}}$  defects) and  $12.0 \pm 1.4\%$  (assuming  $\text{Sn}_{\text{Li}}$  for out-of-plane defects and  $\text{Ir}_{\text{Li}}$  for in-plane defects) after a single cycle between 4.60 and 2.50 V, approximately evenly split between in-plane and out-of-plane antisite defects. Since the total accessed capacity is approximately the same between LIO and the various LISO compositions, by substituting with Sn we can conclude that the structural disordering is not due to global structural instability caused by low lithium contents. Instead, the disordering appears to be associated with the new redox partner giving rise to the high-voltage plateau: the disorder in LISO25 after a full cycle is dramatically greater than in both LIO after the first cycle and LISO25 after a single cycle between 4.25 and 2.50 V, which are both zero within experimental error. Out-of-plane refinement of the fully charged O1 structure shows that the disorder is increased substantially at 4.60 V (Supplementary Tables 3 and 4), providing a direct connection between the new redox partner, electrochemical irreversibility and the onset of cation disordering. Increased cation disordering with increased redox capacity beyond  $\text{Ir}^{4+/5.5+}$  is further supported by pair distribution function (PDF) analysis (Supplementary Figs. 11–14 and Supplementary Table 5) and extended X-ray absorption fine structure (EXAFS) at the Ir  $L_3$  edge (Supplementary Fig. 15), which shows that the decrease in scattering intensity of the first and second coordination shells during charge in LISO—indicative of disorder in the atomic distances—is more substantial when the fraction of capacity beyond  $\text{Ir}^{4+/5.5+}$  is greater (that is, with increasing Sn content). The changes to the XRD pattern in charged LISO50 (Supplementary Fig. 16) are complex and make reliable quantification of occupancies with Rietveld refinement challenging. However, refinement in the discharged state (Supplementary Tables 6 and 7) and the PDF and EXAFS behaviour are similar to, and show more extensive disordering than, those of LISO25. As discussed later, DFT also consistently predicts more favourable in-plane and out-of-plane cation migration in fully charged LISO when compared with LIO, further supporting cation disordering during charging.

### O redox switched on by Sn substitution

The electrochemical and structural data confirm that Sn substitution turns on an additional high-voltage redox partner that is associated with  $M_{\text{Li}}-V_{\text{M}}$  defect formation and voltage hysteresis. To further probe the nature of the high-voltage LISO redox partner, we perform operando transmission XAS at the Ir  $L_3$  and Sn K edges and RIXS at the O K edge. Fig. 3c and Supplementary Fig. 17a show that, as with LIO, charging to 4.25 V results in a shift to higher energy of the Ir  $L_3$  WL energy. This is correlated with an increase in intensity of the Ir  $5d-O 2p t_{2g}$  peak at the O K edge (Fig. 3d), confirming that this is standard hybridized Ir–O redox. Strikingly, the Ir  $L_3$  WL energy is essentially unchanged when charging beyond 4.25 V, exhibiting only a slight decrease in the peak intensity (Supplementary Fig. 17c). As argued previously, the invariance of the Ir  $L_3$  WL is indicative of a constant oxidation state, and thus we rule out continued hybridized Ir–O redox during the high-voltage plateau. Supplementary Figure 17d shows that the Sn K-edge absorption changes minimally during charge in LISO25, ruling out the improbable scenario of Sn oxidation beyond  $4^+$ .

The constant Ir/Sn oxidation states during the high-voltage plateau suggest O redox, and we again turn to the O K-edge XAS/RIXS for confirmation. Fig. 3d shows that, when charging LISO25 from 4.25 to 4.60 V, the  $t_{2g}$  peak continues to increase in intensity despite the invariance of the Ir  $L_3$ -edge WL. This indicates an increased O  $2p$  character in the  $t_{2g}$  band without the depopulation of hybridized Ir–O states. Additionally, Fig. 3e shows that, when charging to 4.60 V, a sharp RIXS feature at 530.7 eV excitation energy and

523.0 eV emission energy (indicated by the white arrows) emerges. This is seen more clearly in the RIXS emission spectra in Fig. 3f. The feature is strongest in LISO50, which exhibits the greatest extent of high-voltage capacity beyond  $\text{Ir}^{4+/5.5+}$  (Fig. 3a) and antisite–vacancy defects. This RIXS feature has been observed to closely follow oxygen redox activity in several battery electrodes<sup>6,31</sup>. Both of these behaviours indicate that, in addition to promoting cation disordering, Sn substitution in LISO also switches on O redox.

### Cation migration and O redox stabilized by LMCT

Understanding why Sn substitution gives rise to these phenomena is central to uncovering the origin of the coupling between anion redox and metal migration–vacancy formation. Since the defect concentration is more reliably quantified in LISO25, we focus our DFT analysis on this composition. First, we show in Supplementary Fig. 18 the evolution of the computed DOS in the control case of ordered,  $M_{\text{Li}}-V_{\text{M}}$ -free LISO25 as a function of Li stoichiometry. We observe that no unhybridized O  $2p$  states are depopulated in the fully delithiated O1 structures—only hybridized Ir–O states are accessed, giving Ir a formal oxidation state of at least  $6^+$ , which is inconsistent with our XAS results. In fact, the behaviour is similar to LIO (albeit more oxidized), with the unhybridized O  $2p$  states positioned about 1 eV below the Fermi level. Thus, simple delithiation and the O3–O1 stacking change does not explain the high-voltage redox process in LISO. Importantly, our DFT calculations suggest that O redox cannot occur in LISO after delithiating  $1.5 \text{ Li f.u.}^{-1}$  if  $M_{\text{Li}}-V_{\text{M}}$  defects are not allowed to form.

Next, we introduce the experimentally observed  $\text{Sn}_{\text{Li}}-V_{\text{M}}$  defects and examine their effect on the electronic structure and charge distribution of LISO. Out-of-plane Sn migration into a Li layer site creates a cation vacancy,  $V_{\text{M}}$ , and neighbouring single-coordinate (dangling) oxygen atoms (Supplementary Fig. 19). Note that we use the term ‘single-coordinate’ to refer to the number of covalent bonding partners—that is counting Ir or Sn, but not Li. We find that the formation of  $\text{Sn}_{\text{Li}}-V_{\text{M}}$  defect pairs stabilizes the delithiated structure significantly by 1.34–1.36 eV, whereas the formation of  $\text{Ir}_{\text{Li}}-V_{\text{M}}$  defect pairs is predicted to have a much smaller driving force of 0.02 eV.

We attribute the  $\text{Sn}_{\text{Li}}-V_{\text{M}}$  stabilization to the response of the resulting M–O dangling bonds, which undergo one of two major transformations. As shown in Fig. 4a, when  $M=\text{Ir}$ , these bonds contract substantially, changing from about 2.10 Å to about 1.77 Å. Fig. 4b shows that the bond contraction accompanies a splitting of the previously unhybridized O  $2p$  states (shaded, top panel), with some states moving above the Fermi level and becoming oxidized (shaded, bottom panel). The shifted states, now approximately 1.5 eV higher in energy, rehybridize with the Ir  $5d$  states. Supplementary Table 8 shows that the bond contraction results in a donation of charge from the dangling oxygens to the Ir bonding partners. Crystal orbital overlap population analysis in Supplementary Discussion 4 and Supplementary Fig. 20 shows that the net bond order between the dangling O and Ir ions increases by 45% as a result. Together, these observations suggest the formation of short Ir–O  $\pi$  bonds (equivalently, terminal oxo ligands) through donation of oxygen lone-pair electrons, approaching Ir=O double bonds although an exact bond order is hard to define in an electronically delocalized crystal. Indeed the substantially shortened Ir–O bonds (1.76–1.79 Å) are similar in length to the Ir=O double bond observed in tetrahedral oxotrimethyliridium(V)<sup>34</sup>. While short Ir–O  $\pi$  bonding in octahedral environments has not been previously observed in molecular compounds, the low effective  $\text{Ir}^{6+} d$  count ( $d^3$ ) makes such bonding possible in charged LISO<sup>35</sup>.

When  $M=\text{Sn}$ , on the other hand, the single-coordinate oxygens are predicted to instead pair up to form short ( $\sim 1.44 \text{ \AA}$ ) O–O dimers that straddle the  $V_{\text{M}}$  (Fig. 4c and Supplementary Fig. 19). Again, this transformation results in a shift of the previously buried

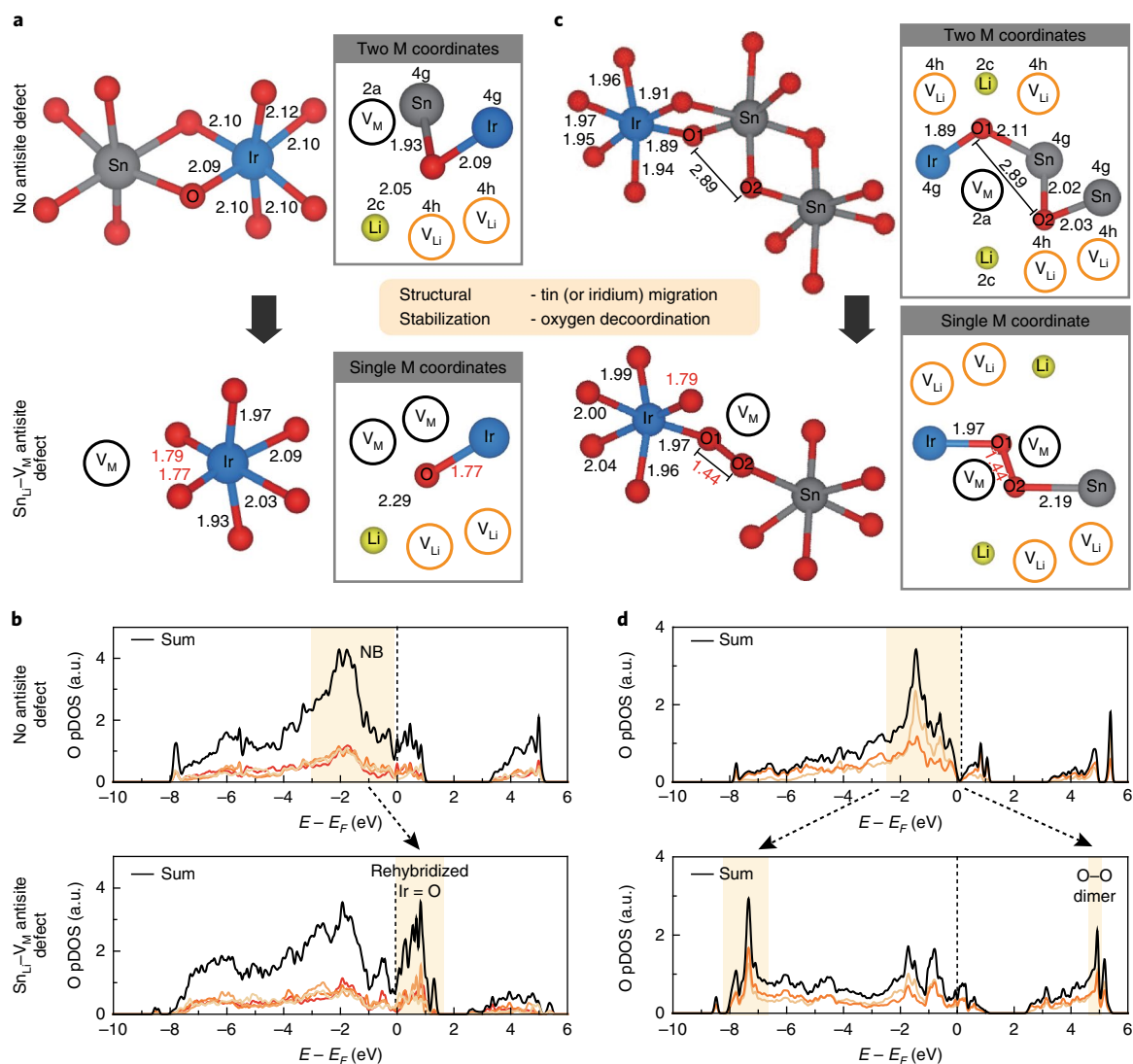


**Fig. 4 | Computational predictions of M-O decooordination and Ir=O/O-O stabilized anion redox.** **a**, Ir-O bond lengths (left) and oxygen coordination environments (right) predicted by DFT in a  $\text{Li}_{0.5}\text{Ir}_{0.75}\text{Sn}_{0.25}\text{O}_3$  structure before and after the formation of a  $\text{Sn}_{\text{Li}}\text{-V}_{\text{M}}$  defect when the vacancy neighbours only Ir. Note that the presence of Li neighbouring O negligibly affects the O 2p states due to minimal hybridization between Li and O. **b**, pDOS of the individual oxygen atoms involved in the Ir-O bond contraction before and after forming the  $\text{Sn}_{\text{Li}}\text{-V}_{\text{M}}$  defect, demonstrating the shift of the O 2p states above the Fermi level, indicating oxygen redox. **c**, Ir-O bond lengths (left) and oxygen coordination environments (right) before and after the formation of a  $\text{Sn}_{\text{Li}}\text{-V}_{\text{M}}$  defect when the migrating Sn initially neighbours another Sn, resulting in the formation of a 1.44 Å O-O dimer. **d**, pDOS of the individual oxygen atoms involved in the O-O bond formation before and after forming the  $\text{Sn}_{\text{Li}}\text{-V}_{\text{M}}$  defect and O-O dimer, also showing a shift of the O 2p states above the Fermi level.

non-bonding O 2p states from below to above the Fermi level (Fig. 4d) along with donation of electron density from O to a neighbouring Ir (Supplementary Table 9). We stress that these localized dimers are distinct from the long (~2.5 Å) dimers previously proposed for this material<sup>15</sup> in that they are well within the range of typical bond lengths for  $\text{O}_2^{n-}$  species<sup>33</sup>, and crucially do not form in the absence of cation migration. These behaviours—the stabilization of the charged structure through Sn migration and Ir=O/O-O formation—are also predicted for LISO50 (Supplementary Fig. 21). We furthermore note that the computational conclusions are independent of the functional employed (Supplementary Table 10).

We note that when both oxygens neighbouring the  $\text{V}_{\text{M}}$  are coordinated to an Ir ion, the short Ir-O  $\pi$  bonds are generally predicted to be more favoured than O-O dimers (Supplementary Fig. 21 and Supplementary Table 10). However, as the Sn content is increased, the fraction of Sn-Sn neighbours increases and thus so does the

fraction of Sn-coordinated dangling oxygens after TM migration–vacancy formation, which favour O–O formation (Supplementary Fig. 21 and Supplementary Table 11). This observation may be due to the increased rotational freedom of the Sn–O bond, facilitating O–O dimerization<sup>5</sup>, as well as the ability of TMs with low d counts (such as  $\text{Ir}^{5+/6+}$ ) to adopt terminal oxo ligands in octahedral environments<sup>35</sup>. In addition, in-plane  $\text{M}_{\text{Li}}/\text{V}_{\text{M}}$  defect pairs can give rise to the same behaviour (Supplementary Fig. 22).

Both the  $\text{V}_{\text{M}}$ -mediated O–O dimer and short Ir–O bond models are consistent with the local structural evolution measured through EXAFS and PDF. EXAFS (Supplementary Fig. 15) shows a substantial decrease in the Ir–O scattering intensity during charge in LISO, which is exacerbated with increasing oxygen redox capacity, consistent with an increased range of Ir–O bond lengths. Meanwhile PDF (Supplementary Fig. 14) shows a broadening of the M–O nearest-neighbour scattering peak in charged LISO, with an increase

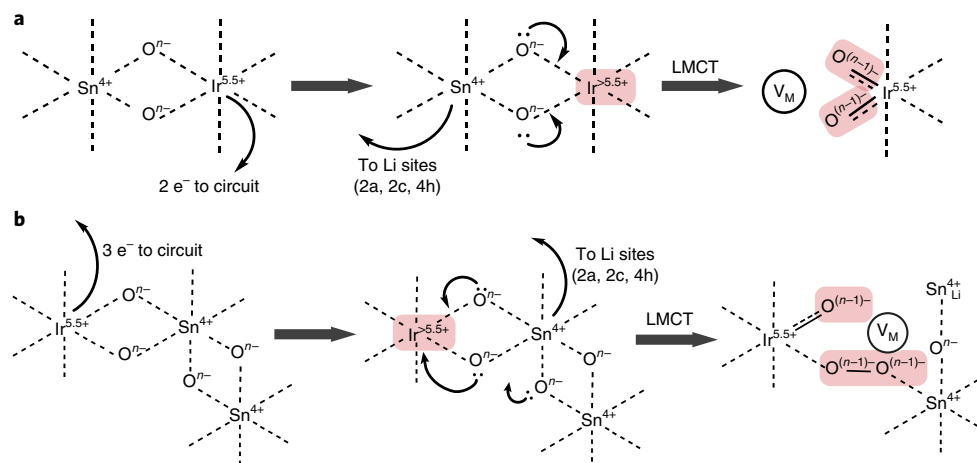


**Fig. 5 | Proposed electronic mechanism of cation migration and LMCT-mediated anion redox in LISO. a**, The mechanism of Ir=O formation, wherein Ir is initially oxidized beyond Ir<sup>5.5+</sup>, promoting LMCT via Sn migration, oxygen decoordination and donation of oxygen lone-pair (unhybridized O 2p) electrons to forming a short Ir–O  $\pi$  bond. Each black arrow corresponds to the redistribution of an electron pair. **b**, The mechanism of O–O formation when a dangling O is coordinated to a Sn atom, wherein LMCT is achieved instead through donation of the O–O  $\sigma^*$  electrons to Ir. Both cases assume that the number of electrons provided through LMCT-mediated oxygen redox is equal to the number of decoordinated oxygens. Note that the calculations in Fig. 4 reflect only the LMCT step in both cases.

in scattering intensity at lower radial distance, consistent with the formation of bonds shorter than the octahedral M–O distance of about 2 Å.

Additionally, both the O–O dimer and short Ir–O bond mechanisms are supported by the spectroscopy data. Fig. 4b predicts the donation of the buried O 2p electrons to the over-oxidized Ir ions by raising these buried states above the Fermi level and into the  $t_{2g}$  band, preventing Ir from exceeding the 5.5<sup>+</sup> oxidation state. This is consistent with the increase in the O K-edge  $t_{2g}$  peak intensity (Fig. 3d) in the absence of a shift in the Ir L<sub>3</sub> WL energy during oxygen redox (Fig. 3c). Meanwhile, the sharp RIXS feature is associated with specific excitations in highly oxidized states, especially those involving unoccupied O 2p states in oxidized oxygen species. Both peroxides<sup>36</sup> and O<sub>2</sub> gas<sup>37</sup> display the same kind of RIXS feature as do charged Li-rich 3d layered oxides<sup>4,6,16,31</sup>. Consistently, the formation of O–O dimers presents a mechanism through which the buried O 2p states may become unoccupied during delithiation in LISO. While our proposal of O–O is consistent with the RIXS result, we cannot rule out the possibility that different types of oxidized oxygen species may also give rise to a similar feature.

Under our earlier definition, the formation of O<sub>2</sub><sup>2-</sup> dimers qualifies as oxygen redox, since as shown in Fig. 4 O 2p states are shifted above the Fermi level (that is depopulated) and end up as the peroxide  $\sigma^*$ , which has mostly oxygen character. Thus, this mechanism serves to localize positive charge onto O 2p orbitals even in an otherwise highly covalent system. However, in the case of forming short Ir–O  $\pi$  bonds, while the O 2p states are again shifted above the Fermi level, they end up rehybridizing with Ir  $t_{2g}$  states. In this case, although this results in additional capacity beyond Ir<sup>4+/5.5+</sup>, the character of these states, and thus the extent to which this counts as oxygen redox, depends on the TM–O hybridization. While the hybridization may be significant in the LISO materials, the nature of such states could be different in less covalent materials, such as 3d TM oxides, and could therefore be important for oxygen redox in other systems.

To understand why LISO undergoes cation migration and oxygen redox while LIO does not, we show in Supplementary Discussion 5 that the driving force for forming Sn<sub>Li</sub>–V<sub>M</sub> defect pairs depends strongly on the electron count in LISO, becoming favourable only when this falls below 1.5 e<sup>-</sup> per Ir less than that of the pristine material. Thus, it is clear that the driving force for this structure–redox

coupling in LISO is the over-oxidation of Ir beyond an average 5.5<sup>+</sup> oxidation state. It is also clear that in the two structural transformations described in Fig. 4 (Ir=O and O–O) substantial donation of charge occurs from O to Ir. It has been shown that in Na-ion battery compounds unusually high oxidation states such as Fe<sup>4+</sup> and Cu<sup>3+</sup> are stabilized by LMCT, wherein a substantial donation of charge from oxygen to the metal centre occurs through strong M–O covalency and low charge transfer energy<sup>38</sup>. We therefore propose that when oxidizing beyond Ir<sup>5.5+</sup> a sufficiently low charge transfer energy is achieved that substantial LMCT is promoted and, consequently, new structural motifs and bonding configurations that allow for greater LMCT become stabilized. In the case of Ir=O the Ir–O bond length is substantially shortened such that the covalency and LMCT is increased (as is clear in Fig. 4b and Supplementary Fig. 20 and is well known, for example, for the Mn=O bonds in KMnO<sub>4</sub><sup>39</sup>), while in the case of O–O electrons are directly transferred from the O–O  $\sigma^*$  to neighbouring Ir ions. Fig. 5 shows the stepwise process schematically: over-oxidation of Ir through delithiation, followed by Sn migration to create either Ir=O or O–O species with a resulting donation of charge back to Ir, with the net result being oxidation of O. Since the predicted O–O dimer bond length is 1.44 Å, we depict these dimers as peroxide species in Fig. 5. Since the average Ir oxidation state never exceeds 5.5<sup>+</sup> in LIO, substantial LMCT is not promoted, and therefore LIO exhibits excellent retention of its in-plane and out-of-plane cation order during cycling and no anion redox.

Thus, the single-coordinate oxygens simultaneously stabilize both the low valence electron count in charged LISO through LMCT and the resulting oxidized oxygen species, whether they settle as terminal oxo ligands or O–O dimers. Consequently, they promote and stabilize the formation of Sn<sub>Li</sub>–V<sub>M</sub> defects. Importantly, this structure–redox coupling quantitatively accounts for the anion-redox capacity. The diffraction results give a V<sub>M</sub> concentration in LISO25 of 12.0 ± 1.4% assuming out-of-plane Sn<sub>Li</sub> defects and in-plane Ir<sub>Li</sub> defects. This extent of disordering is accompanied by an additional redox capacity of about 0.48 Li beyond Ir<sup>4+/5.5+</sup>. Assuming that each decoordinated oxygen contributes one redox electron, this implies that on average about four oxidized oxygens are generated per migrated atom. Each in-plane and out-of-plane migration pathway studied here generates four dangling oxygens, in agreement with this value.



We note that the spectroscopic and structural signature of oxidized oxygen in LISO is strikingly similar to that in  $3d$  and  $4d$  Li-rich layered oxides<sup>6,31</sup>. Further work is needed to establish the precise commonalities between  $3d$ ,  $4d$  and  $5d$  Li-rich electrode materials, in particular the mechanism of decoordination and the relative driving force for forming short M–O  $\pi$  bonds versus short approximately  $1.44 \text{ \AA}$  O–O dimers. However, this initially suggests that depopulation of the high-energy O  $2p$  states lying along the linear Li–O–Li axes of the honeycomb environments in Li-rich layered oxides is generally stabilized through antisite–vacancy formation, short M–O  $\pi$  bonding and/or short O–O dimerization. Indeed, *ab initio* molecular dynamics studies have predicted such mechanisms in  $3d$  Li-rich materials<sup>40</sup>. This also means that the same two-M-coordinate Li–O–Li environments (where M is a covalent, non-alkali cation) that promote oxygen redox by raising the energy of the O  $2p$  states also facilitate its stabilization, as only a single M–Li site swap is required to reach a single M coordinate. In systems such as LISO where these O  $2p$  states are not sufficiently high lying to be depopulated in the disorder-free state, O redox can still occur if the valence electron count is depleted enough for substantial LMCT to be promoted via the formation of antisite–vacancy defects, donating the otherwise inaccessible O  $2p$  electrons to a TM to form the resulting M–O  $\pi$  bonds and O–O dimers.

This mechanism contrasts with the conventional thinking that antisite–vacancy formation in Li-rich layered oxides is driven by the destabilization of the layered structure at low Li stoichiometries<sup>15,41,42</sup>. We instead propose that this defect behaviour is best understood as an overall decoordination of oxygen in response to low valence electron counts and/or oxygen redox. Indeed, this explains why the onset of electrochemical irreversibility for wide a range of Sn content coincides with exceeding the Ir<sup>5.5+</sup> oxidation state and not a specific Li stoichiometry (Fig. 3a). We also emphasize that this decoordination takes the form of both in-plane and out-of-plane cation disorder. This rationalizes early theories of Li-rich layered-oxide structural behaviour, which proposed a conversion of the honeycomb superstructure to a layered LiMO<sub>2</sub> phase via in-plane cation migration<sup>43</sup>, with later studies observing out-of-plane site disorder creating spinel-like structures<sup>41</sup>.

## Conclusion

In summary, by investigating the effect of Sn substitution in the LIO–LISO model system, we have revealed the origin of the strong coupling between anion redox and structural disordering in Li-rich layered oxides that underlies their irreversible electrochemical properties. We find that LIO exhibits no anion redox, and multivalent hybridized Ir–O redox accounts for the entire capacity, reconciling why this material exhibits more reversible electrochemical and structural behaviour than most known anion-redox-active Li-ion electrode materials. Thus, the long approximately  $2.5 \text{ \AA}$  O–O ‘dimers’ that form in LIO during charge are not evidence of anion redox. When Sn is substituted, the lower valence electron count towards the end of charging promotes substantial LMCT through the formation of short Ir–O  $\pi$  bonds and approximately  $1.4 \text{ \AA}$  O–O dimers, requiring the presence of neighbouring cation vacancies and therefore driving the formation of Sn<sub>Li</sub>–V<sub>M</sub> defect pairs. The LMCT realized by the Ir=O and O–O species maintains Ir at its maximum oxidation state of 5.5+ and results, on balance, in O redox. The spectroscopic and structural similarities between O redox in LISO and a range of other Li-rich layered oxides<sup>6,31,44</sup> suggest that oxygen redox may be generally stabilized in the local coordination environments created through local structural defects. Although further study is needed to establish the commonalities between materials, this explanation rationalizes the widespread coupling of oxygen redox to cation disordering that gives rise to its irreversible electrochemical properties.

We expect that the nature of the TM=O and O–O species, along with the kinetics and thermodynamics of forming the M<sub>Li</sub>–V<sub>M</sub>

defect pair, will determine the materials’ voltage, long-term cycling stability and rate capability, offering a new framework in which to optimize the performance of Li-rich electrodes. We further suggest that structures outside the layered Li<sub>1+x</sub>M<sub>1-x</sub>O<sub>2</sub> framework that can accommodate the formation of short O–O and/or TM=O bonds through small distortions rather than substantial cation rearrangement or, alternatively, materials that can achieve substantial LMCT without drastic structural changes (for example through enhanced covalency) could exhibit improved electrochemical and structural reversibility during anion redox. Indeed, in Na-ion layered oxides where interlayer cation migration is limited and possibly even prevented by the large interlayer spacing and/or prismatic interlayer site geometry, structurally reversible anion redox can be achieved<sup>45,46</sup>. Given the stabilizing effect of cation migration demonstrated here, the relative reactivity of these materials towards the electrolyte and oxygen evolution in the absence of cation migration will be an interesting avenue of further study. Our results reveal a clear strategy for designing materials for applications beyond energy storage where low valence electron counts (high oxidation states) need to be reversibly accessed, such as catalysts for reactions including oxygen evolution<sup>20,47,48</sup>, olefin polymerization<sup>49</sup> and methane hydroxylation<sup>50</sup>.

## Online content

Any methods, additional references, Nature Research reporting summaries, source data, statements of data availability and associated accession codes are available at <https://doi.org/10.1038/s41563-018-0276-1>.

Received: 16 April 2018; Accepted: 17 December 2018;

Published online: 04 February 2019

## References

- Whittingham, M. S. Ultimate limits to intercalation reactions for lithium batteries. *Chem. Rev.* **114**, 11414–11443 (2014).
- Assat, G. & Tarascon, J.-M. Fundamental understanding and practical challenges of anionic redox activity in Li-ion batteries. *Nat. Energy* **3**, 373–386 (2018).
- Sathiyaraj, M. et al. Reversible anionic redox chemistry in high-capacity layered-oxide electrodes. *Nat. Mater.* **12**, 827–835 (2013).
- Luo, K. et al. Charge-compensation in  $3d$ -transition-metal-oxide intercalation cathodes through the generation of localized electron holes on oxygen. *Nat. Chem.* **8**, 684–691 (2016).
- Seo, D.-H. et al. The structural and chemical origin of the oxygen redox activity in layered and cation-disordered Li-excess cathode materials. *Nat. Chem.* **8**, 692–697 (2016).
- Gent, W. E. et al. Coupling between oxygen redox and cation migration explains unusual electrochemistry in lithium-rich layered oxides. *Nat. Commun.* **8**, 2091 (2017).
- Zhan, C. et al. Enabling the high capacity of lithium-rich anti-fluorite lithium iron oxide by simultaneous anionic and cationic redox. *Nat. Energy* **2**, 963–971 (2017).
- Assat, G., Delacourt, C., Corte, D. A. D. & Tarascon, J.-M. Editors’ choice—practical assessment of anionic redox in Li-rich layered oxide cathodes: a mixed blessing for high energy Li-ion batteries. *J. Electrochem. Soc.* **163**, A2965–A2976 (2016).
- Sathiyaraj, M. et al. Origin of voltage decay in high-capacity layered oxide electrodes. *Nat. Mater.* **14**, 230–238 (2014).
- Dogan, F. et al. Re-entrant lithium local environments and defect driven electrochemistry of Li- and Mn-rich Li-ion battery cathodes. *J. Am. Chem. Soc.* **137**, 2328–2335 (2015).
- Croy, J. R. et al. Examining hysteresis in composite xLi<sub>2</sub>MnO<sub>3</sub>(1-x)LiMO<sub>2</sub> cathode structures. *J. Phys. Chem. C* **117**, 6525–6536 (2013).
- Kleiner, K. et al. Origin of high capacity and poor cycling stability of Li-rich layered oxides: a long-duration in situ synchrotron powder diffraction study. *Chem. Mater.* **30**, 3656–3667 (2018).
- Abdellahi, A., Urban, A., Dacek, S. & Ceder, G. The effect of cation disorder on the average Li intercalation voltage of transition-metal oxides. *Chem. Mater.* **28**, 3659–3665 (2016).
- Konishi, H. et al. Potential hysteresis between charge and discharge reactions in Li<sub>1.2</sub>Ni<sub>0.13</sub>Mn<sub>0.54</sub>Co<sub>0.15</sub>O<sub>2</sub> for lithium ion batteries. *Solid State Ion.* **300**, 120–127 (2017).

15. McCalla, E. et al. Visualization of O–O peroxo-like dimers in high-capacity layered oxides for Li-ion batteries. *Science* **350**, 1516–1521 (2015).
16. Luo, K. et al. Anion redox chemistry in the cobalt free 3d transition metal oxide intercalation electrode  $\text{Li}[\text{Li}_{0.2}\text{Ni}_{0.2}\text{Mn}_{0.6}]\text{O}_2$ . *J. Am. Chem. Soc.* **138**, 11211–11218 (2016).
17. Kobayashi, H., Tabuchi, M., Shikano, M., Kageyama, H. & Kanno, R. Structure, and magnetic and electrochemical properties of layered oxides,  $\text{Li}_2\text{IrO}_3$ . *J. Mater. Chem.* **13**, 957–962 (2003).
18. Delmas, C., Braconnier, J.-J., Fouassier, C. & Hagemuller, P. Electrochemical intercalation of sodium in  $\text{Na}_x\text{CoO}_2$  bronzes. *Solid State Ion.* **3–4**, 165–169 (1981).
19. Perez, A. J. et al. Approaching the limits of cationic and anionic electrochemical activity with the Li-rich layered rocksalt  $\text{Li}_3\text{IrO}_4$ . *Nat. Energy* **2**, 954–962 (2017).
20. Grimaud, A., Hong, W. T., Shao-Horn, Y. & Tarascon, J. M. Anionic redox processes for electrochemical devices. *Nat. Mater.* **15**, 121–126 (2016).
21. Yabuuchi, N. et al. Origin of stabilization and destabilization in solid-state redox reaction of oxide ions for lithium-ion batteries. *Nat. Commun.* **7**, 13814 (2016).
22. Choy, J.-H., Kim, D.-K., Hwang, S.-H., Demazeau, G. & Jung, D.-Y. XANES and EXAFS Studies on the Ir–O bondcovalency in ionic iridium perovskites. *J. Am. Chem. Soc.* **117**, 8557–8566 (1995).
23. Mugavero, S. J., Smith, M. D., Yoon, W.-S. & zur Loye, H.-C.  $\text{Nd}_2\text{K}_2\text{IrO}_7$  and  $\text{Sm}_2\text{K}_2\text{IrO}_7$ : iridium(VI) oxides prepared under ambient pressure. *Angew. Chem. Int. Ed.* **48**, 215–218 (2009).
24. Laguna-Marco, M. A. et al. Electronic structure, local magnetism, and spin–orbit effects of Ir(IV)-, Ir(V)-, and Ir(VI)-based compounds. *Phys. Rev. B* **91**, 214433 (2015).
25. Qi, B., Perez, I., Ansari, P. H., Lu, F. & Croft, M.  $L_2$  and  $L_3$  measurements of transition-metal 5d orbital occupancy, spin-orbit effects, and chemical bonding. *Phys. Rev. B* **36**, 2972–2975 (1987).
26. Yoon, W.-S. et al. Investigation of the charge compensation mechanism on the electrochemically Li-ion deintercalated  $\text{Li}_{1-x}\text{Co}_{1/3}\text{Ni}_{1/3}\text{Mn}_{1/3}\text{O}_2$  electrode system by combination of soft and hard X-ray absorption spectroscopy. *J. Am. Chem. Soc.* **127**, 17479–17487 (2005).
27. Mortemard de Boisse, B., Liu, G., Ma, J., Nishimura, S.-I. & Chung, S.-C. et al. Intermediate honeycomb ordering to trigger oxygen redox chemistry in layered battery electrode. *Nat. Commun.* **7**, 11397 (2016).
28. Qiao, R. et al. Direct experimental probe of the Ni(II)/Ni(III)/Ni(IV) redox evolution in  $\text{LiNi}_{0.5}\text{Mn}_{0.5}\text{O}_4$  electrodes. *J. Phys. Chem. C* **119**, 27228–27233 (2015).
29. Liu, X. et al. Why  $\text{LiFePO}_4$  is a safe battery electrode: Coulomb repulsion induced electron-state reshuffling upon lithiation. *Phys. Chem. Chem. Phys.* **17**, 26369–26377 (2015).
30. Maitra, U. et al. Oxygen redox chemistry without excess alkali metal ions in  $\text{Na}_{2/3}[\text{Mg}_{0.28}\text{Mn}_{0.72}]\text{O}_2$ . *Nat. Chem.* **10**, 288–295 (2018).
31. Xu, J. et al. Elucidating anionic oxygen activity in lithium-rich layered oxides. *Nat. Commun.* **9**, 947 (2018).
32. Chen, H. & Islam, M. S. Lithium extraction mechanism in Li-rich  $\text{Li}_2\text{MnO}_3$  involving oxygen hole formation and dimerization. *Chem. Mater.* **28**, 6656–6663 (2016).
33. Cramer, C. J., Tolman, W. B., Theopold, K. H. & Rheingold, A. L. Variable character of O–O and M–O bonding in side-on ( $\eta^2$ ) 1:1 metal complexes of  $\text{O}_2$ . *Proc. Natl Acad. Sci. USA* **100**, 3635–3640 (2003).
34. Hay-Motherwell, R. S., Wilkinson, G., Hussain-Bates, B. & Hursthouse, M. B. Synthesis and X-ray crystal structure of oxotrimesityliridium(V). *Polyhedron* **12**, 2009–2012 (1993).
35. Winkler J. R., & Gray H. B. in *Molecular Electronic Structures of Transition Metal Complexes I* (eds Mingos, D. M. P., Day, P. & Dahl, J. P.) 17–28 (Springer, Berlin, 2012).
36. Zhuo, Z. et al. Spectroscopic signature of oxidized oxygen states in peroxides. *J. Phys. Chem. Lett.* **9**, 6378–6384 (2018).
37. Hennies, F. et al. Resonant inelastic scattering spectra of free molecules with vibrational resolution. *Phys. Rev. Lett.* **104**, 193002 (2010).
38. Talaie, E., Kim, S. Y., Chen, N. & Nazar, L. F. Structural evolution and redox processes involved in the electrochemical cycling of  $\text{P2-Na}_{0.67}[\text{Mn}_{0.66}\text{Fe}_{0.20}\text{Cu}_{0.14}]\text{O}_2$ . *Chem. Mater.* **29**, 6684–6697 (2017).
39. Gilbert, B. et al. Multiple scattering calculations of bonding and X-ray absorption spectroscopy of manganese oxides. *J. Phys. Chem. A* **107**, 2839–2847 (2003).
40. Benedek, R. First-cycle simulation for Li-rich layered oxide cathode material  $x\text{Li}_2\text{MnO}_3$  (1-x) $\text{LiMO}_2$  (x=0.4). *J. Electrochem. Soc.* **165**, A2667–A2674 (2018).
41. Mohanty, D. et al. Unraveling the voltage-fade mechanism in high-energy-density lithium-ion batteries: origin of the tetrahedral cations for spinel conversion. *Chem. Mater.* **26**, 6272–6280 (2014).
42. Ceder, G. & Van der Ven, A. Phase diagrams of lithium transition metal oxides: investigations from first principles. *Electrochim. Acta* **45**, 131–150 (1999).
43. Thackeray, M. M. et al.  $\text{Li}_2\text{MnO}_3$ -stabilized  $\text{LiMO}_2$  (M=Mn, Ni, Co) electrodes for lithium-ion batteries. *J. Mater. Chem.* **17**, 3112–3125 (2007).
44. Okubo, M. & Yamada, A. Molecular orbital principles of oxygen-redox battery electrodes. *ACS Appl. Mater. Interfaces* **9**, 36463–36472 (2017).
45. Mortemard de Boisse, B. et al. Highly reversible oxygen-redox chemistry at 4.1 V in  $\text{Na}_{4/7-x}[\square_{1/7}\text{Mn}_{6/7}]\text{O}_2$  ( $\square$ :Mn vacancy). *Adv. Energy Mater.* **8**, 1800409 (2018).
46. Rong, X. et al. Structure-induced reversible anionic redox activity in Na layered oxide cathode. *Joule* **2**, 125–140 (2018).
47. Surendranath, Y., Kanan, M. W. & Nocera, D. G. Mechanistic studies of the oxygen evolution reaction by a cobalt-phosphate catalyst at neutral pH. *J. Am. Chem. Soc.* **132**, 16501–16509 (2010).
48. Grimaud, A. et al. Activating lattice oxygen redox reactions in metal oxides to catalyse oxygen evolution. *Nat. Chem.* **9**, 457–465 (2017).
49. Billow, B. S., McDaniel, T. J. & Odom, A. L. Quantifying ligand effects in high-oxidation-state metal catalysis. *Nat. Chem.* **9**, 837–842 (2017).
50. Snyder, B. E. R. et al. The active site of low-temperature methane hydroxylation in iron-containing zeolites. *Nature* **536**, 317–321 (2016).

## Acknowledgements

This research was supported by the Assistant Secretary for Energy Efficiency and Renewable Energy, Office of Vehicle Technologies, Battery Materials Research Program, US Department of Energy (DOE). W.E.G. was supported additionally by the Advanced Light Source Doctoral Fellowship and the Siebel Scholars programme. K.L. was supported additionally by the Kwanjeong Education Foundation Fellowship. Use of the ALS was supported by the Office of Science, Office of Basic Energy Sciences, of the US DOE under contract no. DE-AC02-05CH11231. Use of the SSRL, SLAC National Accelerator Laboratory, was supported by the Office of Science, Office of Basic Energy Sciences, of the US DOE under contract no. DE-AC02-76SF00515. Work at the Molecular Foundry was supported by the Office of Science, Office of Basic Energy Sciences, of the US DOE under contract no. DE-AC02-05CH11231. Part of this work was performed at the Stanford Nano Shared Facilities, supported by the National Science Foundation under award ECCS-1542152. This research used resources of the APS, an Office of Science User Facility operated for the US DOE Office of Science by Argonne National Laboratory, and was supported by the US DOE under contract no. DE-AC02-06CH11357, and the Canadian Light Source and its funding partners. The computational work was funded by the NorthEast Center for Chemical Energy Storage, an Energy Frontier Research Center, supported by the US DOE, Office of Science, Office of Basic Energy Sciences under award no. DE-SC0012583. G.C. also thanks the China Automotive Battery Research Institute and the General Research Institute for NonFerrous Metals for financial support on oxygen redox in cathode materials. **W.E.G. thanks Ariel Jacobs for insightful discussions on metal–oxygen bonding interactions.** The authors thank Karena Chapman (APS) for valuable comments on X-ray total scattering analysis.

## Author contributions

J.H., W.E.G., W.C.C. and M.F.T. conceived the study. J.H. carried out materials synthesis, characterization and testing. J.H. and K.L. performed ex situ and operando synchrotron measurements including XRD, PDF, XAS, sXAS and RIXS. J.H. and W.E.G. measured ex situ STXM and RIXS spectra. W.E.G., J.W. and W.Y. processed and analysed spectroscopic data. K.L., J.H., K.H.S., D. Passarello and M.F.T. performed the structural analyses. K.L., J.H., C.J.T., M.F.T. and W.C.C. designed and constructed settings for in situ synchrotron measurements. P.X., D.-H.S. and G.C. conducted DFT calculations. J.W., K.H.S., D.N., C.-J.S. and K.L. configured synchrotron end stations. P.M.C. provided constructive advice for experiments. J.H., W.E.G., D. Prendergast, W.C.C. and M.F.T. devised the oxygen redox model. J.H., W.E.G., G.C., W.C.C. and M.F.T. wrote the manuscript and all authors revised the manuscript.

## Competing interests

The authors declare no competing interests.

## Additional information

**Supplementary information** is available for this paper at <https://doi.org/10.1038/s41563-018-0276-1>.

**Reprints and permissions information** is available at [www.nature.com/reprints](http://www.nature.com/reprints).

**Correspondence and requests for materials** should be addressed to G.C., M.F.T. or W.C.C.

**Publisher's note:** Springer Nature remains neutral with regard to jurisdictional claims in published maps and institutional affiliations.

© The Author(s), under exclusive licence to Springer Nature Limited 2019

## Methods

**Materials.** LIO, LISO25 and LISO50 were synthesized by solid-state reactions. Appropriate amounts of  $\text{Li}_2\text{CO}_3$  (Alfa Aesar, 99.998% metal basis),  $\text{IrO}_2$  (Alfa Aesar, 99.99% metal basis) and  $\text{SnO}_2$  (Alfa Aesar 99.9% metal basis) were mixed using a planetary ball mill. A 10% excess of  $\text{Li}_2\text{CO}_3$  was used to compensate the lithium evaporation at high temperature. Mixed powder was heat treated at 1000 °C for 12 h twice in a box furnace with an intermittent grinding, and then naturally cooled to room temperature.

**Electrochemical measurements and electrode harvesting.** For all electrochemistry figures in this study, 80 wt.% active material, 10 wt.% polyvinylidene fluoride (PVDF) binder (MTI Corporation) and 10 wt.% carbon black (Timcal C65) were mixed with *N*-methyl-2-pyrrolidone (Acros Organics) and the slurry was cast onto carbon-coated Al foil using a doctor blade. The electrode sheet was dried at 110 °C in air for 1 h then overnight at 60 °C under vacuum. Coin cells (CR2032, Wellcos) were assembled in an Ar-filled glove box with an approximately 11.3 mm diameter LIO–LISO electrode, two 25  $\mu\text{m}$  thick Celgard separators, a 750  $\mu\text{m}$  thick Li-foil counter-electrode (Sigma-Aldrich) and 1 M  $\text{LiPF}_6$  in 1:1 (v/v) ethylene carbonate–diethyl carbonate electrolyte (Selectlyte LP 40, BASF). The coin cells were cycled under a constant current density of a C/12 rate (1 C = 211 mA per  $g_{\text{LIO}}$ , 227.4 mA per  $g_{\text{LISO25}}$ , 246.6 mA per  $g_{\text{LISO50}}$  corresponding to the (de)lithiation rate of 2  $\text{Li h}^{-1}$  f.u. $^{-1}$ ) between 4.60 V and 2.50 V (LIO and LISO) or 4.25 V and 2.50 V (LISO). The galvanostatic intermittent titration technique was applied to measure the open-circuit voltage at various states of charge and the thermodynamic voltage hysteresis of LIO and LISO. We applied constant current pulses (C/20) for 1 h followed by relaxation for 4 h. This was repeated until the galvanostatic intermittent titration technique cycle was complete.

Ex situ sXAS (FY), XRD and RIXS samples were dismantled from coin cells at the indicated states of charge in an Ar-filled glove box. Cells were dismantled using a coin-cell decrimping instrument (MTI). The electrodes were then rinsed with excess diethyl carbonate and dried under vacuum in the glove-box antechamber. For XRD, materials were scraped off of the Al-foil current collector and then sealed in a glass capillary (0.5 mm diameter, Ted Pella). All the samples were transferred to the desired instrument in a double-sealed Al-coated polypropylene pouch to prevent air exposure.

**XRD and Rietveld refinement.** High-resolution powder XRD patterns for Rietveld refinement were measured at beamline 2-1 at the Stanford Synchrotron Radiation Lightsource (SSRL, SLAC National Accelerator Laboratory) at 17 keV (0.7293 Å) beam energy for as-synthesized powders and at beamline 11-ID-B at the Advanced Photon Source (APS, Argonne National Laboratory) at 58.4 keV (0.2114 Å) beam energy for ex situ samples scraped out of electrodes after electrochemical cycling. The size of the X-ray beam was 500 × 1500  $\mu\text{m}^2$  (SSRL) or 500 × 500  $\mu\text{m}^2$  (APS). All of the samples were prepared in capillaries to avoid possible preferred orientation of the particles. All of the samples were measured using the transmission geometry.

We used the TOPAS software package (Academic v6, Bruker) for Rietveld refinement. Pawley fitting was employed to determine the crystallographic parameters. The pristine samples and the samples fully charged to 4.60 V were refined with the *C2/m* space group following previous reports<sup>15</sup>. For the T3-Li<sub>1-x</sub>Ir<sub>x</sub>O<sub>3</sub>, we found the *Cm* space group to give the best results. For LISO, we assumed that Ir and Sn are randomly distributed through the 4h sites in the TM layer, and the migrated Ir/Sn from 4h was assumed to redistribute equally to the 4g and 2c sites in the Li layer. We allowed variations in the Ir occupancy in the Li layer of the fully charged (4.60 V) and fully discharged (2.50 V) LIO and confirmed no Ir migration during the first cycle in LIO.

**X-ray total scattering and PDF analysis.** Atomic PDF was analysed to gain further insights on the local atomic structures of LIO and LISO of the pristine powder and the samples scraped out of the electrodes charged to 4.60 V and discharged to 2.50 V. X-ray total scattering was collected at beamline 11-ID-B at the APS at 58.4 keV (0.2114 Å) beam energy. All of the samples were packed in Kapton capillaries double sealed in an Al-coated pouch in an Ar-filled glove box, and then transferred to the beamline. The pouch was opened right before the measurement to minimize the air exposure. The data collection time was 3 min per sample. We used PDFgetX2 to obtain the atomic PDF from the total scattering data and PDFGUI to fit the atomic PDF from the starting crystal structures determined by Rietveld refinement described above.

**Operando Ir L<sub>3</sub> edge XAS and EXAFS spectroscopy.** For operando XAS, Al-coated polypropylene pouch cells containing an approximately 11.3 mm diameter LIO–LISO electrode, two 25  $\mu\text{m}$  thick Celgard separators, a 250  $\mu\text{m}$  thick Li-foil counter-electrode (Alfa Aesar) and 1 M  $\text{LiPF}_6$  in 1:1 (v/v) ethylene carbonate–diethyl carbonate electrolyte (Selectlyte LP 40, BASF), a Ni negative current-collector tab and an Al positive current-collector tab were assembled using a tabletop vacuum impulse sealer (Fuji Impulse) in an Ar-filled glove box. A stainless-steel holder with a pair of Be plates (Ted Pella) as an X-ray window was machined to apply a sufficient pressure on the pouch cells using torque screws. The pressure from the stiff windows significantly improved electronic conduction throughout the micro-porous electrodes, ensuring homogeneity. The pouch cells

were cycled using a portable potentiostat (SP-150, Biologic) under a constant current density of C/12 (where 1 C refers to 2  $\text{Li h}^{-1}$  f.u. $^{-1}$ ) between 4.60 V and 2.50 V (versus Li) with 1 h rest between charge and discharge.

The Ir L<sub>3</sub>-edge XAS spectra of LIO and LISO were collected at beamline 2-2 of SSRL at SLAC National Accelerator Laboratory and beamline 20-BM of the APS at Argonne National Laboratory, respectively. The transmission spectra were measured using a 1 × 7 mm<sup>2</sup> unfocused X-ray beam. A Si(220) (SSRL) or Si(111) (APS) crystal monochromator was detuned to 70% of its original intensity to eliminate high-order harmonics. Three ion chambers filled with N<sub>2</sub> gas were used in series to simultaneously measure  $I_0$ ,  $I_i$  and  $I_{\text{ref}}$ . A Ge reference foil was used to calibrate the photon energy by setting the peak of the first derivative of the K-edge absorbance spectrum as 11,102 eV, 10 eV, 0.5 eV and 10 eV energy steps were used in the ranges of 10,985–11,085 eV, 11,085.5–11,124.5 eV and 11,125–11,195 eV, respectively, in order to precisely measure the reference Ge K-edge spectra for the calibration followed by the Ir L<sub>3</sub>-edge measurement. We used the Athena software package to align and normalize the collected spectra. The WL peak was fitted using the sum of an error function and a Lorentzian peak analogous to previous reports. Fourier transformations of  $k^2$ -weighted EXAFS spectra were carried out in the  $k$  range from 2 Å<sup>-1</sup> to 14 Å<sup>-1</sup> for all the materials.

**O K-edge sXAS: FY, RIXS and transmission.** O K-edge sXAS of the harvested electrodes was measured in FY mode at SSRL beamline 10-1 equipped with a silicon photodiode detector (AXUV100). Data was acquired under ultrahigh vacuum (10<sup>-9</sup> Torr) at room temperature with an incident X-ray beam of size 500 × 500  $\mu\text{m}^2$ .

RIXS maps were collected at beamline 8.0.1 at the Advanced Light Source (ALS) in Lawrence Berkeley National Laboratory, using the ultrahigh-efficiency iRIXS endstation. All the harvested electrodes were sealed in Al pouches in an Ar-filled glove box, and transferred into a specially designed transfer kit and then the experimental vacuum chamber to avoid air exposure. Technical details of the RIXS beamline and data processing can be found in our previous reports<sup>65,61</sup>. Two-dimensional emission spectra collected at each excitation energy are aligned using the elastic peak and a reference compound such as TiO<sub>2</sub> to generate the full RIXS maps. The colour scale has been tuned in the figures to emphasize the contrast of intensity.

Transmission O K-edge sXAS was measured at ALS beamline 11.0.2 using STXM. The samples were prepared by sonicating the harvested electrodes in dimethyl carbonate under Ar for 2 h at room temperature to separate individual particles out of the composite electrodes. The particle suspension was drop-cast onto copper transmission electron microscopy grids with a carbon film (Ted Pella). The grids were loaded onto a sample holder, sealed in an Al-coated pouch, and then transferred to the beamline. We first collected the STXM images with a 50 nm zone plate, an interferometer-controlled stage and a point detector. The step size was 50 nm and the dwell time for each pixel was typically 1 ms. STXM spectro-images were aligned in the aXis2000 software package. To obtain average absorption spectra, the aligned absorbance images were filtered at an energy of non-zero intensity, typically 529.5 eV. The pixels below a threshold intensity were set to zero. The remaining un-normalized pixels were then summed to yield the average spectrum. For presentation, normalization of the average spectra was done by subtracting the background intensity and then dividing by the post-edge intensity.

**Computational details.** The calculations for all structures presented were performed with DFT as implemented in the Vienna Ab initio Simulation Package (VASP)<sup>32,33</sup>. Valence electrons were described by the plane-wave basis set and core electrons were incorporated by the projector augmented-wave method<sup>34–37</sup>. Unless otherwise indicated, the Perdew–Burke–Ernzerhof (PBE) functional<sup>38</sup> with the Hubbard *U* correction<sup>39</sup> was adopted for the exchange correlation energy. An effective *U* value of 2.75 eV was applied to Ir<sup>6+</sup>. For hybrid calculations, the Heyd–Scuseria–Ernzerhof (HSE) screened Coulomb hybrid density functional<sup>61</sup> was used with a mixing parameter of 0.15 and a range separation parameter of 0.2<sup>62</sup>. The energy cutoff of the plane wave basis was 520 eV and the  $k$ -point mesh was 3 × 3 × 7 for a 2 × 2 × 1 supercell of O3-Li<sub>2-x</sub>Ir<sub>x</sub>MO<sub>3</sub>. The van der Waals interactions were taken into account using the D2 method of Grimme<sup>63</sup> for PBE + *U* and HSE calculations. For SCAN calculations, the rVV10 non-local van der Waals correlation functional was used<sup>64</sup>. To prepare the structures of Li<sub>2-x</sub>Ir<sub>x</sub>O<sub>3</sub>, we generated all Li-vacancy orderings within the unit cell of Li<sub>2-x</sub>Ir<sub>x</sub>O<sub>3</sub> including four f.u. using the enumeration technique developed by Hart et al.<sup>65,66</sup>, and 10 configurations at  $x = 1.5$  and 0.5 and 100 configurations at  $x = 1$  with the lowest electrostatic energy were calculated using the generalized gradient approximation (GGA). The configurations with the lowest DFT/GGA energy at each Li content were selected as the most stable structures. Both octahedral and tetrahedral sites in the Li layer within O3- and O1-Li<sub>2-x</sub>Ir<sub>x</sub>O<sub>3</sub> were considered for Li-vacancy orderings at  $x = 1$ . The same Li-vacancy orderings were applied to the Li<sub>2-x</sub>Ir<sub>0.75</sub>Sn<sub>0.25</sub>O<sub>3</sub> case. After Sn migration to the Li layer, the Li-vacancy orderings were re-sampled using the basin hopping algorithm<sup>67</sup>.

## Data availability

All experimental data within the article and its Supplementary Information will be made available upon reasonable request to the authors.

## References

51. Chuang, Y.-D. et al. Modular soft x-ray spectrometer for applications in energy sciences and quantum materials. *Rev. Sci. Instrum.* **88**, 013110 (2017).
52. Kresse, G. & Hafner, J. *Ab initio* molecular dynamics for liquid metals. *Phys. Rev. B* **47**, 558–561 (1993).
53. Kresse, G. & Hafner, J. *Ab initio* molecular-dynamics simulation of the liquid–metal amorphous–semiconductor transition in germanium. *Phys. Rev. B* **49**, 14251–14269 (1994).
54. Kresse, G. & Furthmüller, J. Efficient iterative schemes for *ab initio* total-energy calculations using a plane-wave basis set. *Phys. Rev. B* **54**, 11169–11186 (1996).
55. Kresse, G. & Furthmüller, J. Efficiency of *ab-initio* total energy calculations for metals and semiconductors using a plane-wave basis set. *Comput. Mater. Sci.* **6**, 15–50 (1996).
56. Blöchl, P. E. Projector augmented-wave method. *Phys. Rev. B* **50**, 17953–17979 (1994).
57. Kresse, G. & Joubert, D. From ultrasoft pseudopotentials to the projector augmented-wave method. *Phys. Rev. B* **59**, 1758–1775 (1999).
58. Perdew, J. P., Burke, K. & Ernzerhof, M. Generalized gradient approximation made simple. *Phys. Rev. Lett.* **77**, 3865–3868 (1996).
59. Dudarev, S. L., Botton, G. A., Savrasov, S. Y., Humphreys, C. J. & Sutton, A. P. Electron-energy-loss spectra and the structural stability of nickel oxide: an LSDA+U study. *Phys. Rev. B* **57**, 1505–1509 (1998).
60. Subedi, A. First-principles study of the electronic structure and magnetism of CaIrO<sub>3</sub>. *Phys. Rev. B* **85**, 020408 (2012).
61. Heyd, J., Scuseria, G. E. & Ernzerhof, M. Hybrid functionals based on a screened Coulomb potential. *J. Chem. Phys.* **118**, 8207–8215 (2003).
62. Seo, D.-H., Urban, A. & Ceder, G. Calibrating transition-metal energy levels and oxygen bands in first-principles calculations: accurate prediction of redox potentials and charge transfer in lithium transition-metal oxides. *Phys. Rev. B* **92**, 115118 (2015).
63. Grimme, S. Semiempirical GGA-type density functional constructed with a long-range dispersion correction. *J. Comput. Chem.* **27**, 1787–1799 (2006).
64. Peng, H., Yang, Z.-H., Perdew, J. P. & Sun, J. Versatile van der Waals density functional based on a meta-generalized gradient approximation. *Phys. Rev. X* **6**, 041005 (2016).
65. Hart, G. L. W. & Forcade, R. W. Algorithm for generating derivative structures. *Phys. Rev. B* **77**, 224115 (2008).
66. Hart, G. L. W., Nelson, L. J. & Forcade, R. W. Generating derivative structures at a fixed concentration. *Comput. Mater. Sci.* **59**, 101–107 (2012).
67. Wales, D. J. & Doye, J. P. K. Global optimization by basin-hopping and the lowest energy structures of Lennard-Jones clusters containing up to 110 atoms. *J. Phys. Chem. A* **101**, 5111–5116 (1997).